Ultrasensitive guided-mode resonance biosensors superimposed with vertical-sidewall roughness

Chih-Sheng Jao and Hoang Yan Lin*

Institute of Photonics and Optoelectronics and Department of Electrical Engineering, National Taiwan University, Taipei 10617, Taiwan

*Corresponding author: hylin@cc.ee.ntu.edu.tw

Received 28 March 2011; revised 8 July 2011; accepted 12 July 2011; posted 18 July 2011 (Doc. ID 144884); published 8 September 2011

In this paper, we present our investigations of the effects of vertical-sidewall roughness (VSR) on guided-mode resonance (GMR) filters made of subwavelength grating for applications to ultrasensitive biosensors operated under IR illumination. We designed the spectral FWHM of the grating filter to be as narrow as possible in order to emphasize the sensitivity and VSR effects. Three types of VSR morphologies on the grating—in terms of the correlation length ξ and the rms of the maximum roughness deviation σ—were considered and evaluated. Rigorous coupled-wave analysis was then implemented to quantify the shifts in the reflective resonance peak wavelength value (PWV) of the grating filter. Our simulations show that for specific ξ values, the PWVs remain constant even if σ becomes as large as 10 nm; this indicates dramatic bandgaplike stripes, which are similar to the bandgaps observed in the band diagrams of photonic crystals in the ξ–σ diagram that we have proposed in this study. In other words, the effects of VSR on the GMR biosensor performance are insignificant when ξ is located at certain bands; therefore, this type of roughness is highly tolerable even if the linewidth of the filter is decreased to only a few tens of nanometers.

OCIS codes: 050.1950, 050.5745, 220.3740, 240.5770.

1. Introduction

In the last decade, considerable attention has been focused on guided-mode resonance (GMR) applications to micro-optical elements such as polarizers, filters, and dielectric mirrors [1]. Owing to the simplicity of the geometrical structure, the fabrication of GMR filters is relatively easier than that of conventional filters in which multilayer stacking of thin-film deposition is used. Magnusson and Ding extended the principle of the GMR filter by reviewing the "second stopband theory" and simplified it to a one-layer subwavelength grating that can be more easily diversified to become various diffractive optical elements, such as narrow bandpass polarized filters, narrow bandstop polarized filters, broadband AR coatings [1,2], and broadband polarized mirrors [3]. Cunningham *et al.* [4,5] utilized the characteristics of the ultranarrow band of GMR filters to detect the interactions of 0.1 nm thick protein in which only subnanometer shifts in the peak wavelength value (PWV) can still be told apart. Wang *et al.* [6] experimentally demonstrated that sensor resolutions of a refractive index unit (RIU) are achievable up to accuracies as high as 0.001 to 0.0001. Furthermore, Lee *et al.* [7] designed a sensor in which shifts in the PWV of 0.15 nm per percentage of relative humidity (RH) can be measured when the RH varies from 20% RH to 80% RH. In recent years, considerable attention has shifted to the applications of GMR filters to biosensors because of their unique properties, such as being label-free, high throughput, and compact integration. A comprehensive review of this subject has been provided by Magnusson *et al.* [8].

The abovementioned subwavelength GMR sensors are typically fabricated by using large-area optical interference lithography, nanoimprint lithography, and electron-beam lithography [8–10]. Among these fabrication processes, large-area optical interference

0003-6935/11/265139-10$15.00/0

lithography is the most efficient method for implementing commercialized mass production of biosensors; however, it always introduces vertical-sidewall roughness (VSR) that results from the standing-wave exposure or etching processes, and, moreover, the VSR does not scale down as the linewidth of the grating shrinks [11]. Similarly, the line edge roughness is also a critical issue in current semiconductor processes, particularly when the linewidth is shrunk to only a few tens of nanometers [12]. Although the GMR grating mechanism is based on photons rather than electrons, from the viewpoint of the ultrasensitive characteristics of biosensors, the VSR may lead to possible erroneous judgments. Therefore, careful calibrations are necessary to guarantee the stability, repeatability, and reproducibility of biosensors. Although numerous researches have explored the effects of roughness on semiconductor fabrication, studies on subwavelength GMR ultrasensitive biosensors are relatively few because of the complicated boundary conditions of the three-dimensional (3D) morphology of the roughness in electromagnetic scattering problems. Schuster *et al.* [13] developed a field-stitching method to simplify the complicated boundary conditions of the roughness on the nanoscale grating to accelerate the computing speed, while Bergner *et al.* [14] developed an effective medium theory to reduce the 3D line edge roughness to two-dimensional (2D) problems and thereby avoided extensive computations. Talneau *et al.* [15] explored the impact of imperfections due to electron-beam lithography on the performances of 2D GMR filters and found that 2.5 nm electron-beam writing resolutions (fabrication errors) are still tolerable. Further, Poutous *et al.* [16] reported the results of simulations and fabrications of GMR filters with correlations to lithographic variability, e.g., photoresist exposure dosage and etching depth. Therefore, Schuster and Bergner have only dealt with the line edge roughness on common gratings that are unrelated to GMR gratings, while Talneau and Poutous have merely investigated fabrication errors in GMR filters without mentioning roughness issues. Prasad *et al.* [17] showed that GMR filters are very tolerant to irregularities and interface roughness, but they concentrated only on roughness of the μm scale. Thus far, to our knowledge, the effects of the VSR on GMR biosensors have not been numerically investigated and quantified.

In this study, instead of using a complicated 3D model, we have considered VSR in the vertical-sidewall direction (along the grating depth) and focused only on 2D morphologies to explore its inherent physics. We have proposed an improved model of GMR grating with narrow FWHM. On the one hand, our model is "ultrasensitive" to detect samples, while on the other hand, it is susceptible to VSR; hence, we have to explore its side effects.

This paper is organized as follows: first, we will review the rigorous coupled-wave analysis (RCWA) method used to solve the scattering problem of VSR in Section 2.A. We will then demonstrate the developed GMR biosensor in Sections 2.B and 2.C. Third, the mathematical VSR model is discussed in Section 2.D, and the simulation results with VSR are demonstrated in Section 2.E; finally, we will state our conclusions in Section 3.

2. Simulation Models, Results, and Discussion

A. RCWA Method

In RCWA, the computation domain of the grating model is divided into three regions, as shown in Fig. 1. Region 1 is above the grating region (modulated refractive index region) and contains both reflective and incident electromagnetic fields. Region 2 is the modulated grating region in the middle domain. Region 3 is below the modulated region at which the transmitted electromagnetic field exits. The modulated refractive index can be decomposed as a Fourier series given by Eq. (1) as follows:

$$\varepsilon(x) = \sum_i \varepsilon_i \exp^{j\frac{2\pi i x}{p}}, \tag{1}$$

where ε_i is the ith Fourier-series coefficient of the modulated grating region and p is the grating period. The electromagnetic fields are also decomposed as plane waves by using the Bloch–Floquet theorem [18–20]. Finally, the phase-matching conditions are applied to solve the eigenvalue problem and hence obtain the Fourier coefficients and the distributions of the electromagnetic fields.

B. Ultrasensitive GMR Biosensor Design

Figure 1 shows the schematic structure of the GMR sensor designed for this study. It has been improved from [21], which had required three types of materials; and here it is simplified to contain only two materials. Our target is to obtain a GMR biosensor

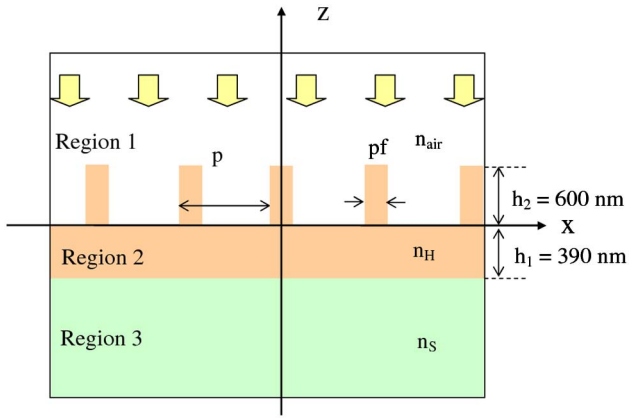

Fig. 1. (Color online) Schematic illustration of the GMR sensor structure discussed in this study. The parameters are as follows: $h_1 = 390$ nm, waveguide layer thickness; $h_2 = 600$ nm, grating height; $p = 900$ nm, grating period; $f = 0.1$, fill factor within the period; $n_H = 1.97$, refractive index of Si_3Ni_4 in both waveguide and grating layers; $n_S = 1.44$, refractive index of SiO_2 in the substrate layer; and the plane wave is in normal incidence.

with a narrower FWHM and make it more sensitive to external perturbations than the previous design [21]. The logic of our design is to use fewer materials in order to simplify the fabrication process and then adjust the parameters, such as the fill factor and period, to make the FWHM narrower. The parameters we use here are illustrated in Fig. 1. The spectral responses of the transverse magnetic (TM, with magnetic field normal to the incident plane) and transverse-electric (TE, with electric field normal to the incident plane) polarizations of the designed biosensor are calculated as shown in Fig. 2. The PWV of the TE polarization is located at 1529 nm while that of the TM polarization is located at 1412.3 nm. The FWHMs of the TE and TM spectra are 3.6 nm and 0.34 nm, respectively. In the previous design [21], the FWHMs of the TE and TM spectra were 9.3 nm and 6.5 nm, respectively. Obviously, our improved design has narrower FWHMs irrespective of the TE and TM spectra. From Fig. 2, the FWHM of the TM polarization in this design is almost 20 times smaller than that of the previous design [21]. Here, the filling factor f of the GMR grating is first scanned for searching for the minimum of FWHM. This strategy can also be explained from the coupling term, $\sin(\pi f/\pi)$, of the coupled-wave equation in Ref. [22], and the extent of mode coupling is strongly related to the fill factor f that is essential to manipulate the FWHM.

Furthermore, the deviation in PWV between TE and TM polarizations is 116.7 nm, which is larger than that (85.8 nm) in the previous design [21]. Larger PWV deviations between the TE and TM polarizations make the measured spectral response more significant, especially when spectroscopic ellipsometry is used. In Figs. 3(a) and 3(b), the adjusted fill factors and the spectra for TM and TE polarizations are shown. The FWHMs broaden for both polarizations when the fill factor approaches 0.5, and they shrink when the fill factor approaches either 0 or 1. The PWVs of both the TM and TE polarizations experience a redshift when the fill factor increases from 0 to 1. This redshift can be qualitatively explained by the concept of effective medium theory, that is, by regarding the modulated grating region as an equivalent layer of thin film. The wavelength becomes shorter in a dense material; i.e., the effective refractive index of the grating increases when the fill factor approaches 1. Consequently, the working wavelength should become longer to match the shortened wavelength in the grating region. On the contrary, the wavelength naturally becomes longer in sparse materials wherein the effective refractive index of the grating is lower because the fill factor approaches 0. Moreover, when the fill factor is larger than 0.9 or less than 0.1, the PWV disappears at some fill factors. For the TM polarization, the FWHM broadens gradually when the fill factor changes from 0 to 0.3; and the PWV appears to redshift quickly along the asymptote at which the fill factor equals 0.5. From Figs. 3(a) and 3(b), we discovered that when the fill factor is below 0.1 or beyond 0.9, the FWHM is sufficiently narrow. Besides, the FWHM for the TM polarization is narrower than that for the TE polarization. The GMR sensor with narrow FWHM can act like a tiny probe to detect samples. However, in such cases, the PWV disappears at some fill factors, and it may be very difficult for current technologies to fabricate such narrow ridges or slits; hence, we have excluded these two extreme conditions.

In Figs. 4(a) and 4(b), the spectra of the TM and TE polarizations are shown, respectively, after the period has been adjusted. The PWVs of both polarizations show proportional redshifts with increasing period. The redshift means the increase of PWV due to the increasing period and can be explained by the scaling principle when the grating material under consideration is nondispersive [3]. In this study,

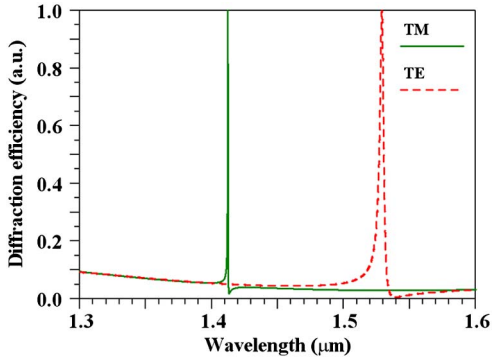

Fig. 2. (Color online) Reflective spectral responses of TM and transverse-electric TE polarizations for the GMR sensor parameters shown in Fig. 1.

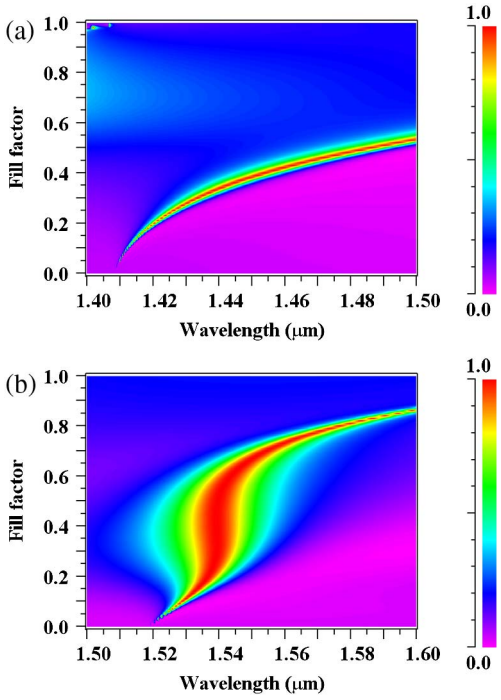

Fig. 3. (Color online) Reflective spectral responses of (a) TM and (b) TE when fill factor changes from 0 to 1 (the grating period is fixed at 900 nm). The color scale represents the reflective intensity.

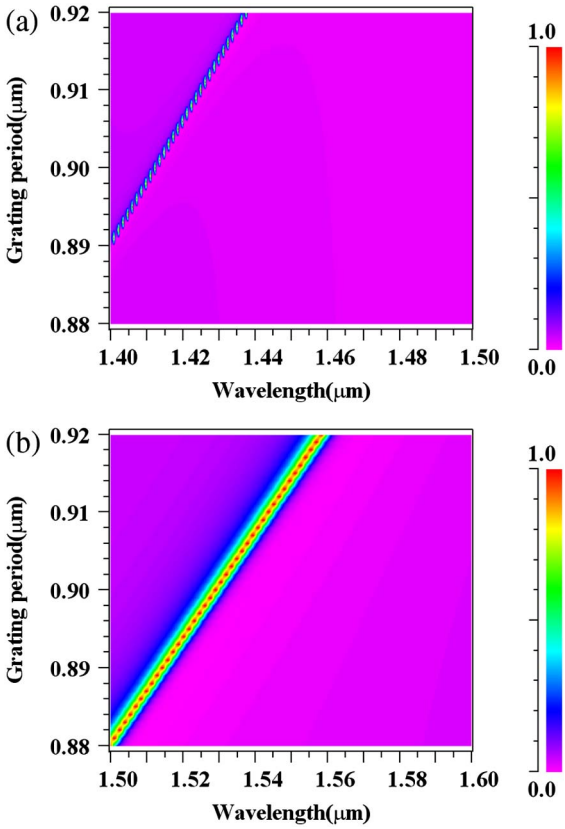

Fig. 4. (Color online) Reflective spectral responses of (a) TM and (b) TE when the period changes from 0.88 to 0.92 (the fill factor of the grating is fixed at 0.1). The color scale represents the reflective intensity.

we have chosen the spectroscopic light source as an incident plane wave. Moreover, the FWHM of the spectrum is very narrow (only 0.34 nm) in our design; therefore, it is reasonable to regard the GMR grating material as nondispersive, especially in the IR range. Consequently, we can also predict the desired PWV by tuning the period and fill factor simultaneously. In addition, we can obtain the PWV with additional parametric variables (e.g., grating depth or thickness of waveguide layer) by employing optimization methods such as genetic algorithms or particle swarm optimization methods. Figs. 5(a) and 5(b) demonstrate the magnetic and electric field amplitudes, respectively, of the GMR sensor at PWV. The size of the calculated domain is $0.9\,\mu\text{m} \times 6\,\mu\text{m}$. The incident plane wave has unit amplitude, and the standing-wave patterns are generated by combining both incident and reflective fields. The TM polarization exhibits stronger field enhancement of 100 times, and this is larger than that in the TE polarization wherein the field enhancement is only 20 times. Detailed magnetic and electric field amplitude distributions along the z axis at $x = 0$ are shown in Figs. 5(c) and 5(d) for a more detailed investigation. A highly enhanced field exists in the waveguide layer between the grating and substrate. The evanescent wave can be used to interact with samples when penetrating into the grating layer. Besides, TM polarization has much larger enhanced mode confinement than TE polarization, as shown in Fig. 5, and has inherently narrower FWHM than TE due to the matching of the boundary condition on the one-dimensional (1D) polarization-dependent grating [22].

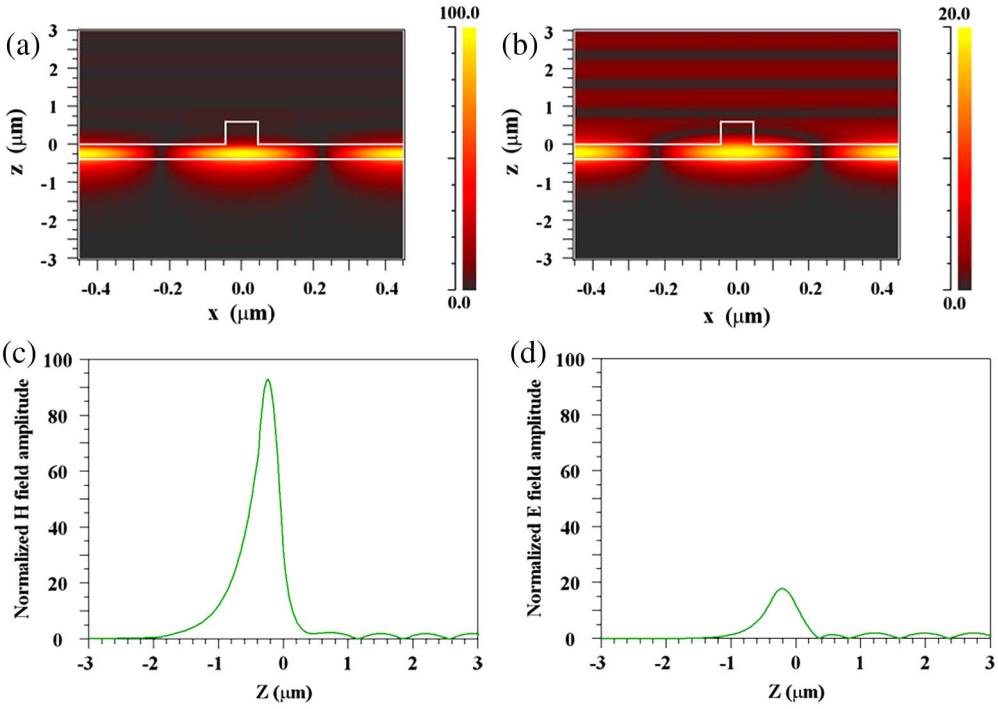

Fig. 5. (Color online) Demonstration of (a) magnetic amplitudes of TM and (b) electric field amplitudes of TE for the GMR sensors at resonance as the field approaches maximum reflectance. The size of the region is $0.9\,\mu\text{m} \times 6\,\mu\text{m}$. Detailed (c) magnetic amplitudes of TM and (d) electric field amplitudes of TE plots for the cross section at $x = 0$.

C. Validation of Ultrasensitive GMR Biosensor

In order to demonstrate that our GMR grating model is capable of being an ultrasensitive candidate, we performed computational experiments on this sensor covered with a virtual biolayer and liquid. Figs. 6(a) and 6(b) show the spectral responses of the TM and TE polarizations when the GMR sensor was covered by a virtual biolayer whose thickness was varied from 0.1 nm to 1 nm. The refractive index of the biolayer was assumed to be 1.5. For TM and TE polarizations, the shifts in PWV were 0.43 nm and 0.3 nm, respectively, for the biolayer thickness of 1 nm; clearly, TM polarization was more sensitive than TE polarization. Moreover, as the thickness of the biolayer increased from 0.1 nm to 1 nm, the PWV shift linearly increased by 0.04 nm per 0.1 nm thickness increment for the TM polarization. However, the PWV shift linearly increased only by 0.03 nm per 0.1 nm thickness increment for the TE polarization; that is, the TE polarization is really less sensitive than the TM one. In fact, the resolution of the present commercial optical spectrum analyzer (OSA), employed in the GMR biosensor system, can reach picometer (i.e., 0.001 nm) levels. Based on this feasibility, our numerical resolution of the output spectrum is reasonably set to 0.01 nm. Once a practical OSA reaches higher resolutions, we can set the numerical resolution of the output spectrum to smaller units, but the massive computational time is unavoidable when finer meshes are employed in RCWA. Figs. 6(c) and 6(d) show the spectral responses of the TM and TE polarizations for the GMR sensor covered by liquid alcohol (refractive index: 1.36–1.361111); here, the alcohol volume was full of upper semi-infinite space. The refractive index is assumed to

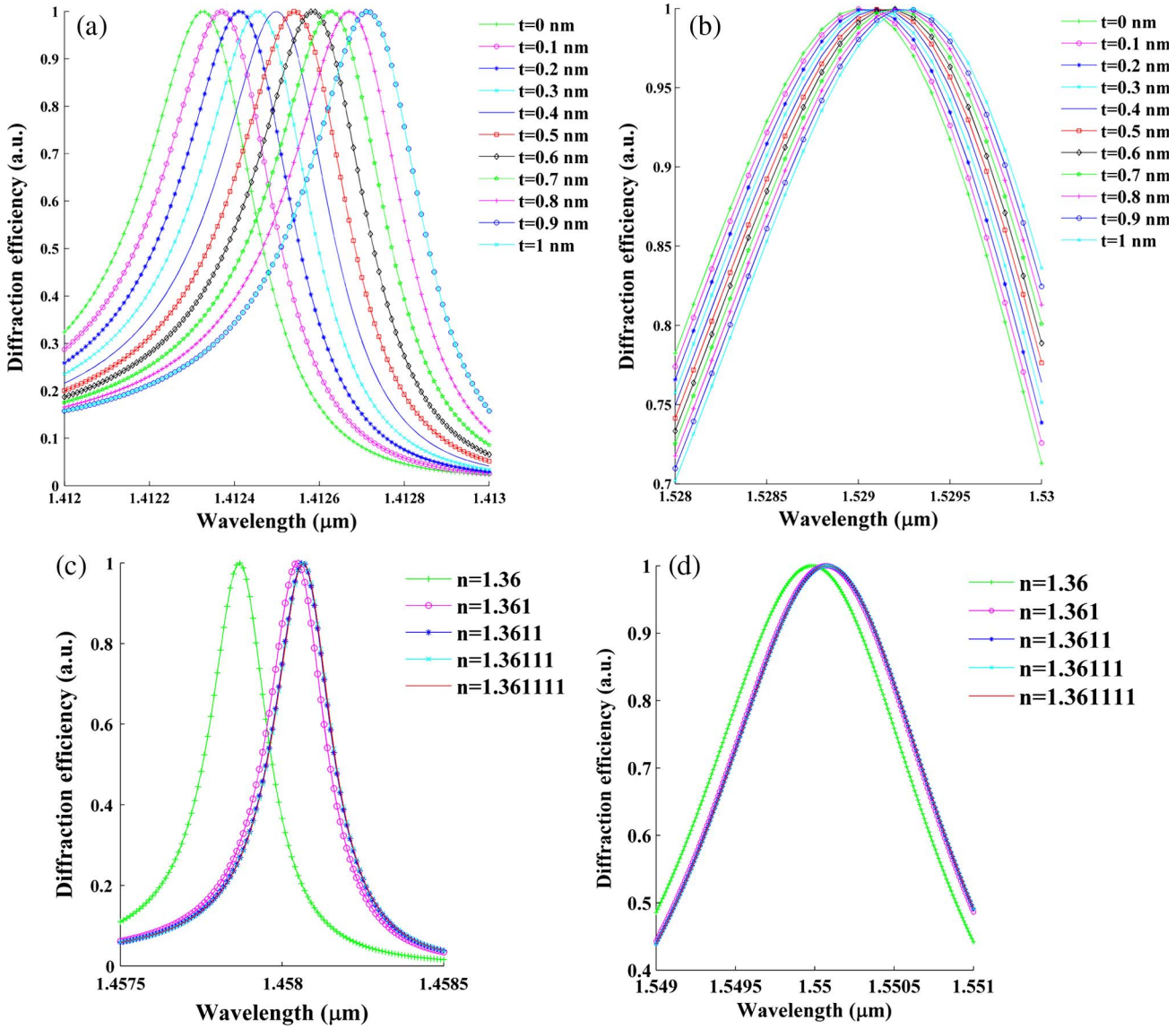

Fig. 6. (Color online) Spectral responses of (a) TM and (b) TE polarizations when the GMR sensor is covered by a virtual biolayer with t varied from 0.1 to 1 nm and with refractive index $n_{\mathrm{bio}} = 1.5$; the spectral responses of (c) TM and (d) TE polarizations when the GMR sensor is covered by liquid alcohol with the refractive index n varied from 1.36 to 1.361111 and the alcohol is full of the upper semi-infinite space.

change with the alcoholic concentration (mol/L) in practice. For TM and TE polarizations, the PWV shifts were 45.77 nm and 21.08 nm, respectively, for the refractive index of the liquid of 1.361111. Similarly, the TM polarization was better than the TE polarization while detecting the perturbation of the refractive index of a liquid.

For the TM polarization, when the refractive index is changed from 1.36111 to 1.361111, the sensor can still be used to distinguish tiny deviations as the refractive index changes down to 0.0001. Similarly, the lower limit of the resolution of the refractive index change detection for the TE polarization can reach at least 0.001. Consequently, hypothetical changes of RIU measured by our biosensor [calculated from Figs. 6(c) and 6(d) by $\Delta\lambda/\Delta n$] can reach a theoretical ultrasensitivity of 1000 nm/RIU and 100 nm/RIU for TM and TE polarization, respectively. Ref. [6] concluded that sensor sensitivity better than 0.001–0.0001 RIU is sufficient to detect various biochemical samples and also mentioned that the state-of-the-art biosensor could reach 2000 nm/RIU of ultrasensitivity. Besides, the biosensor in Ref. [4], with resolution of 112 nm/RIU, is recognized to be highly sensitive. In this study, our design is comparable to the state-of-the-art biosensor with ultrasensitivity, and we have made further investigation of the side effects of VSR for degrading its ultrasensitivity.

D. Characterization of VSR Model

Some of the literature has suggested complex mathematical models to fully characterize the roughness [23]; however, we chose a simple model that uses only two independent parameters—correlation length, ξ, and rms of the maximum roughness deviation, σ—to describe the roughness. These two parameters comprise an autocorrelation function that characterizes the fluctuations in the roughness. The autocorrelation function $A(\mu)$ of a roughness fluctuation $h(z)$ of the VSR is defined as follows: [24]:

$$A(\mu) = \int_{-\infty}^{\infty} h(z)h(z-\mu)\mathrm{d}z. \tag{2}$$

The coordinates of x and z are shown in Fig. 1. The autocorrelation function $A(\mu)$ is applied to define the fluctuations in the roughness between $h(z)$ and $h(z\text{-}\mu)$ at which z is shifted by a distance μ. The rms of the maximum roughness deviation σ is then defined as $A(0)^{1/2}$. Based on Fourier transformation theory, $A(\mu)$ approaches zero as μ approaches infinity, while $A(\mu)$ reaches a maximum as μ approaches zero. Therefore, we provide an assumed autocorrelation function in the analytical form of a power spectral density function as follows:

$$A(\mu) = \sigma^2 \exp^{-\frac{|\mu|}{\xi}}. \tag{3}$$

The correlation length of the specific VSR is defined as ξ in Eq. (3). As the variable correlation length μ equals ξ in Eq. (3), $A(\mu)$ reduces to $\sigma^2(1/e)$. From signal processing theory, we certainly know that fluctuating $h(z)$ is still correlated within this correlation length ξ [24]. The Fourier transform of $A(\mu)$ is then derived as follows [23,25,26], in order to obtain the Fourier components of $h(z)$:

$$W(k) = \int A(\mu)e^{ik\mu}\mathrm{d}\mu. \tag{4}$$

The VSR along the z direction can then be generated from the inverse Fourier transform of the square root of $W(k)$, as shown by the following equation:

$$h(z) = \int W(k)^{1/2}e^{(-ikz)}\mathrm{d}k. \tag{5}$$

Here, k is the spatial frequency of the VSR.

In this study, we generally demonstrate the illustrative distributions of the VSR on the two vertical sidewalls of the grating, as shown in Fig. 7(a). Figure 7(b) shows the random VSR with the same correlation length ξ of 5 nm and with various σ values of 1 nm, 2.5 nm, and 5 nm, while Fig. 7(c) shows the random VSR with σ of 1 nm and with various correlation lengths ξ of 5 nm, 10 nm, and 50 nm. Larger σ results in larger fluctuations in the VSR, whereas longer correlation lengths lead to slower fluctuations.

E. Analysis of GMR Biosensors Superimposed with VSR

In our original GMR sensor design, the PWV of the TM polarization is located at 1412.3 nm while that of the TE polarization is located at 1529 nm with both reflectances close to 100%. We use these PWVs of the original design as a reference to measure their PWV shifts when ξ or σ changes. In Fig. 8, the horizontal and vertical axes are σ and ξ, respectively. The value of each point on the figures represents the reflectance at PWV. The ξ–σ diagram shows that a higher σ implies lower reflectance in the form of blue-stripe regions. However, for several correlation lengths [e.g., $\xi = 92$, 75, 60, 50, 40, 34, 15, and 5 nm in Fig. 8(a) and $\xi = 87$, 74, 55, 47, 40, 30, 18, and 9 nm in Fig. 8(b)], the PWV remains constant (nearly 100%) in the red-stripe region. In these slender red-stripe regions, the incident light was reflected totally, or, in other words, the incident light was unable to penetrate the grating. It is well known that in photonic crystals, the bandgap is the condition under which light cannot propagate forward at certain incident directions and wavelengths. Similarly, the slender red-stripe regions are analogous to these bandgaps. A GMR grating is actually a type of 1D photonic crystal, and hence we can also consider the slender red-stripe regions in the ξ–σ diagram to be bandgaplike regions. The red-stripe region in Fig. 8(b) for TE polarization is wider than that in Fig. 8(a) for TM polarization, but this does not imply that the TE polarization has greater fabrication tolerance for σ than the TM polarization. Conversely, the TE polarization is less sensitive to both VSR

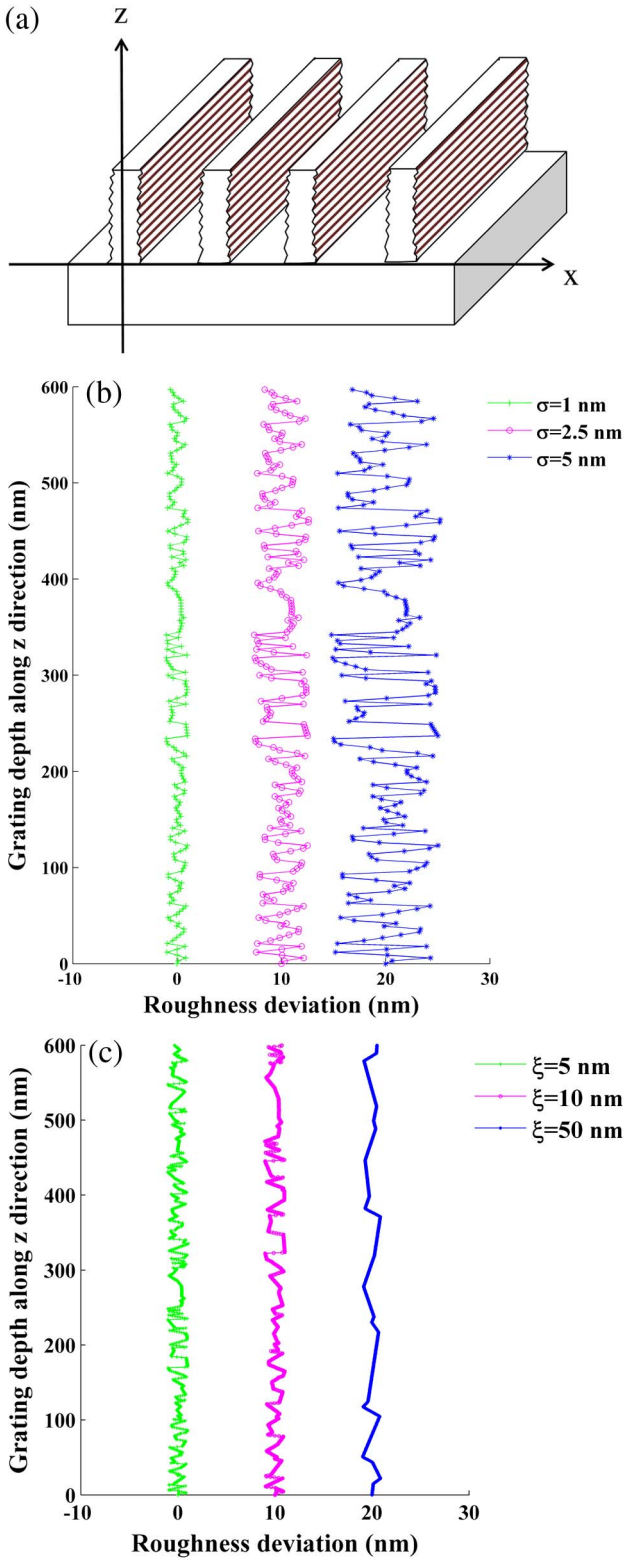

Fig. 7. (Color online) (a) Configuration of the VSR distributed in the GMR biosensor. (b) Demonstration of the random VSR morphology at a fixed correlation length, $\xi = 5$ nm, with various values of rms of roughness σ. (c) Demonstration of the random VSR morphology at a fixed rms of roughness, $\sigma = 1$ nm, with various correlation lengths ξ.

and measured samples. Moreover, TE is also less sensitive to the biolayers or liquids used for measurements, which we have validated in Section 2.D. Further analysis based on Fig. 8(a) was conducted by obtaining spectral responses with increasing ξ at different σ (e.g., $\sigma = 1$, 2.5, 3.5, and 5 nm), and the results can be seen from Figs. 9(a)–9(d). For example, since $\sigma = 1$ nm in Fig. 9(a), the PWV shifts slightly vary within 0.1 nm. For $\sigma = 5$ nm in Fig. 9(d), the shifts in PWV fluctuate strongly and have a maximum of 0.3 nm. We quantify the PWV shifts in these four figures and summarize that the maximum PWV shifts are 0.3 nm when $\sigma = 5$ nm in Fig. 9(d). Even a tiny VSR of $\sigma = 1$ nm will result in 0.1 nm PWV shifts, which are sufficiently large to cause erroneous recognitions in the biolayer sensing described in Subsection 2.B; needless to say, once the PWV shift of 0.3 nm is caused by VSR with $\sigma = 5$ nm.

To investigate the reasons for the VSR resulting in the bandgaplike regions, we also used sinusoidal corrugations, $\sigma \cdot \sin(2\pi z/\xi)$, to represent the VSR for the other simulations. Figures 10(a) and 10(b) show results identical to those in Fig. 8 for the TM and TE polarizations, respectively. From the above results, we can infer that certain modulated spatial distributions of VSR will support the GMR effect; hence, the constructive interferences of incident and reflected waves still exist at some correlation lengths even if σ increases to exceed 10 nm. This specific

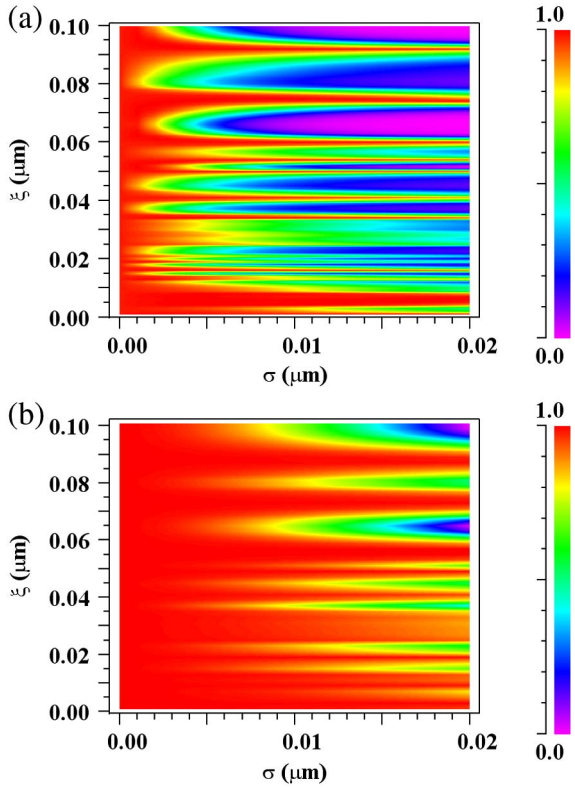

Fig. 8. (Color online) ξ–σ diagram of reflectance at the designed PWV for random VSR. (a) TM and (b) TE polarizations with changes in correlation lengths ξ and rms of roughness σ.

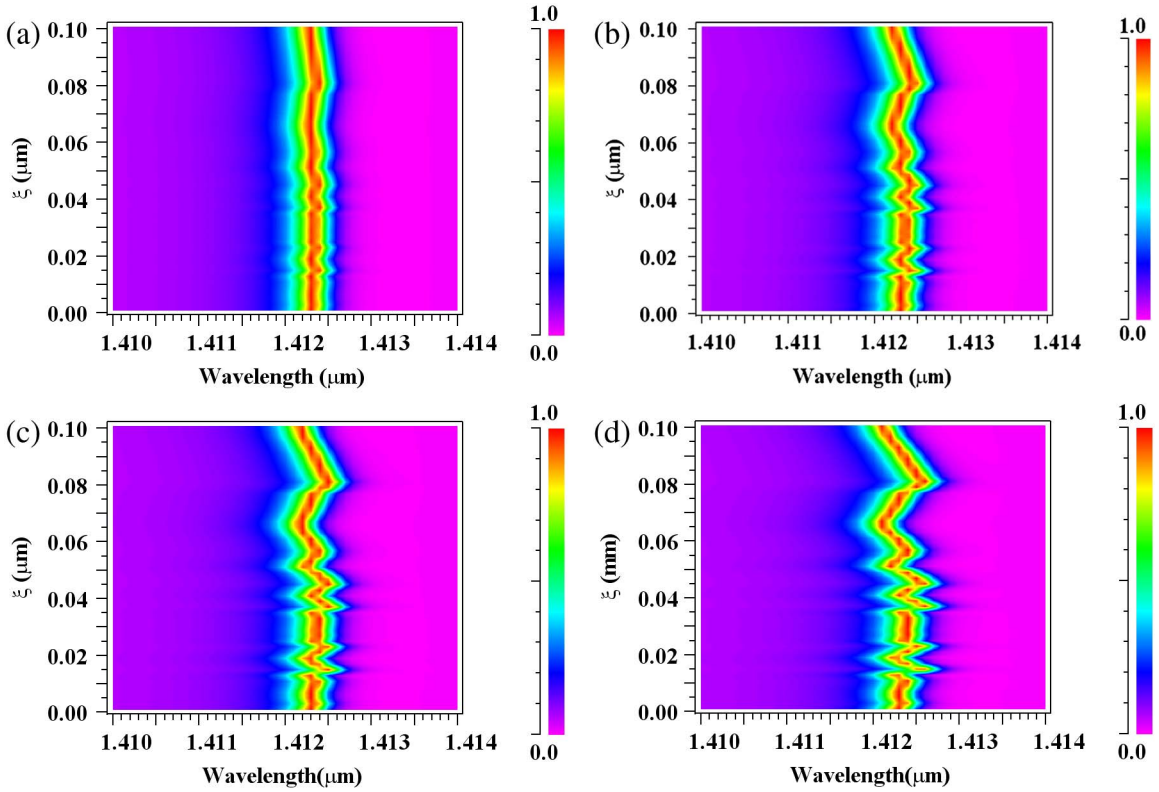

Fig. 9. (Color online) Spectral responses at different values of rms of roughness: (a) $\sigma = 1$ nm, (b) 2.5 nm, (c) 3.5 nm, and (d) 5 nm, with variations in the correlation length ξ.

spatially modulated distribution of the VSR leads to bandgaplike regions. Fortunately, if the ξ–σ parameters fall within the bandgaplike region, the reflectance will be nearly 100%. This is advantageous when the fabrication parameters are controlled within this dramatic bandgaplike region, since larger roughness can then be tolerated.

In contrast, if there were no spatially modulated variations, i.e., when the VSR is regarded as an effective thin-film layer (for computational simplicity), the existence of the anomalous bandgaplike phenomena is interesting. We regard σ and ξ of the random and sinusoidal VSR as the equivalent thickness and period of variation on the effective thin film, respectively [27]. Because the thickness of the VSR considered here is much shallower (maximum: 5 nm) than the grating line width, the higher-order approximations of the effective medium are necessarily assumed to describe the VSR. The zero-order effective indices in three axial directions are as follows:

$$n_{x0} = n_{y0} = n_o = \sqrt{n_{\text{air}}^2(1-f) + f n_R^2}, \tag{6}$$

$$n_{z0} = n_e = \frac{n_{\text{air}} n_R}{\sqrt{n_{\text{air}}^2(1-f) + f n_R^2}}. \tag{7}$$

The second-order effective indices in three axial directions are as follows:

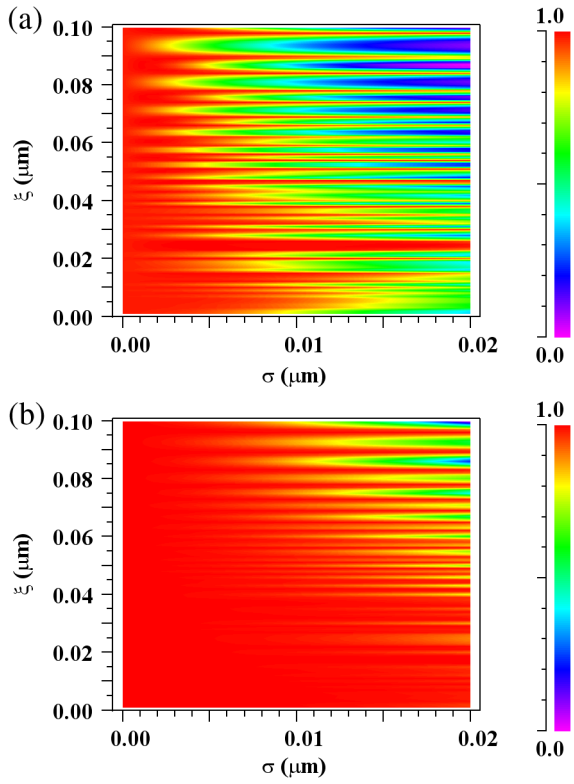

Fig. 10. (Color online) ξ–σ diagram of reflectance at the designed PWV for sinusoidal VSR. (a) TM and (b) TE polarizations with changes in correlation lengths ξ and rms of roughness σ.

$$n_{x2} = n_{y2} = \left\{ n_o^2 + \frac{1}{3}\left[\frac{\pi f(1-f)\xi}{\lambda}\right]^2 (n_R^2 - n_{\text{air}}^2)^2 \right\}^{1/2}, \quad (8)$$

$$n_{z2} = \left\{ n_e^2 + \frac{1}{3}\left[\frac{\pi f(1-f)\xi}{\lambda}\right]^2 \left(\frac{1}{n_R^2} - \frac{1}{n_{\text{air}}^2}\right)^2 n_e^6 n_o^2 \right\}^{1/2}. \quad (9)$$

Here λ is the incident wavelength; n_{air} is the refractive index of the air; n_R is the refractive index of the VSR corrugations; f is the fill factor; and ξ is the period of variation of the VSR corrugations (we have assumed f as a fixed average equal to 0.5 in this study). In our study, the light source is in normal incidence, and hence only n_{x0} and n_{y0} are considered for TM and TE polarizations, respectively. If the incidence is oblique, n_x, n_y, and n_z should be considered simultaneously by tensor transformations. Similar simulations were implemented, and the results are shown in Figs. 11(a) and 11(b). Figure 11 shows the equivalent diagram of PWV shifts in (a) TM and (b) TE polarizations with changes in the equivalent thickness versus the correlation length. Bandgaplike regions do not exist anymore, as we can see from Figs. 8 and 9.

Further analysis based on Fig. 11 to obtain spectral response with varying effective thicknesses and correlation length is shown in Fig. 12. Figs. 12(a) and 12(b) show the redshifts in the PWV with increasing effective correlation length of the VSR in TM and TE polarization, respectively. In both the polarizations, the PWV shift does not fluctuate with the effective correlation length at fixed effective thicknesses; further, the PWV shift varies monotonically. This implies that when the VSR is regarded as an effective medium in terms of effective medium approximations (EMAs), the periodicity of the VSR is eliminated. However, EMAs can still be applied to other line edge roughness or surface roughness in subwavelength grating structures [14]. Since it is known that the periodic grating forms the 1D photonic crystal and leads to GMR effects under some special physical conditions, the unwanted VSR could be inherently decomposed into numerous periodic nanostructures. Therefore, the GMR grating superimposed with VSR is a combination of two kinds of periodic nanostructures in different dimensional scales; for example, the GMR grating has a linewidth of 90 nm, and the VSR has $\sigma = 5$ nm. Thus far, such studies on compound complex nanostructures have been limited, to our knowledge. Further studies are required either to estimate the roughness effects or to realize future nanophotonic applications.

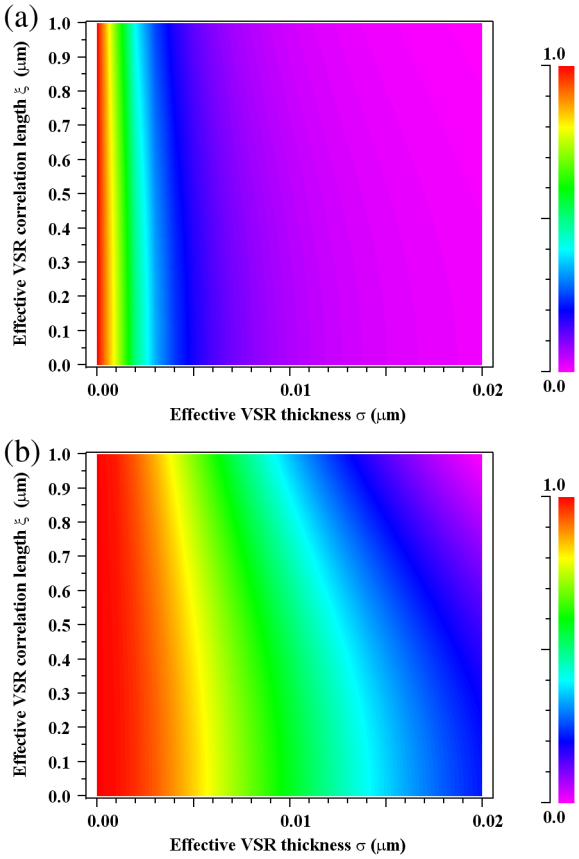

Fig. 11. (Color online) ξ–σ diagram of reflectance at the designed PWV for effective VSR. (a) TM and (b) TE polarizations with changes in correlation lengths ξ and rms of roughness σ.

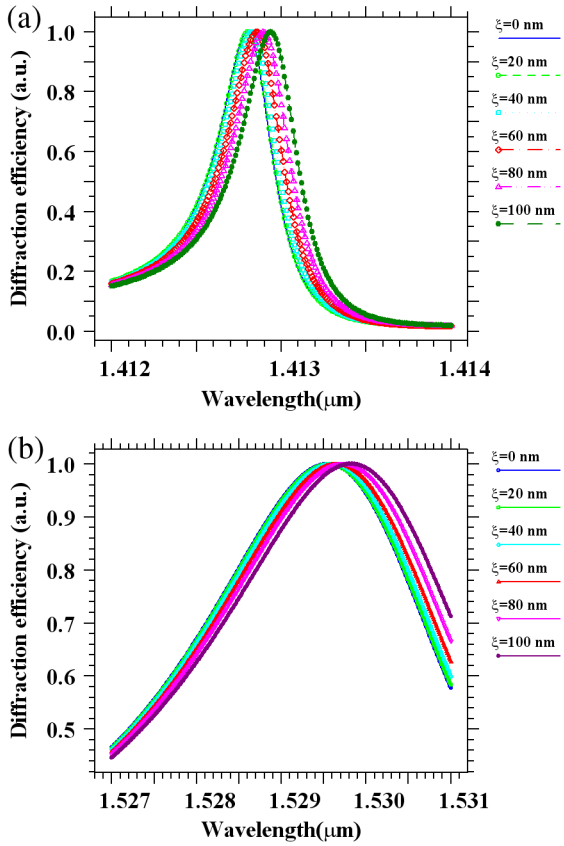

Fig. 12. (Color online) (a) TM and (b) TE polarization showing the redshifts of PWV that increase with the correlation length ξ, respectively.

3. Conclusions

We have proposed an improved simple design for GMR biosensors under IR illumination. Furthermore, we implemented the RCWA approach to explore the effects of VSR on such biosensors, and this is the first such computational experiment to our knowledge. Both TM and TE polarized illuminations are examined. The TM polarization is considerably more sensitive than the TE polarization when the external variations in either the biolayer or liquid are detected. Similarly, TM polarization is also more sensitive to the VSR. Even a tiny VSR of $\sigma = 1\,\mathrm{nm}$ will result in 0.1 nm shifts in PWV, and this is sufficiently large to cause erroneous recognitions in this ultrasensitive biosensor. Fortunately, the PWV shift remains approximately constant at certain ranges of the correlation length of VSR leading to significant bandgaplike phenomena even if the maximum roughness deviations σ are up to 10 nm. Since the random roughness fluctuations can be regarded as the superposition of periodic Fourier-series components, we also discovered that the pseudoregular sinusoidal VSRs have identical bandgaplike phenomena. Based on these facts, if the fabrication conditions can be controlled within these specific ξ values, the side effects of VSR can be largely tolerated in future designs even when the linewidth of the grating is decreased to only a few tens of nanometers.

The authors gratefully acknowledge financial support by the National Science Council of the Republic of China under projects NSC-99-2221-E-002-140 and NTU under the Aim for Top University Project. C. S. Jao also gratefully thanks Dr. Yu-Tang Chen and Dr. An-Cheng Ruo for helpful discussions.

References

1. Y. Ding and R. Magnusson, "Resonant leaky-mode spectral-band engineering and device applications," Opt. Express **12**, 5661–5674 (2004).
2. Y. Ding and R. Magnusson, "Use of nondegenerate resonant leaky modes to fashion diverse optical spectra," Opt. Express **12**, 1885–1891 (2004).
3. C. F. R. Mateus, M. C. Y. Huang, Y. Deng, A. R. Neureuther, and C. J. Chang-Hasnain, "Ultrabroadband mirror using low-index cladded subwavelength grating," IEEE Photon. Technol. Lett. **16**, 518–520 (2004).
4. B. Cunningham, B. Lin, J. Qiu, P. Li, J. Pepper, and B. Hugh, "A plastic colorimetric resonant optical biosensor for multiparallel detection of label-free biochemical interactions," Sens. Actuators B **85**, 219–226 (2002).
5. B. Cunningham, P. Li, B. Lin, and J. Pepper, "Colorimetric resonant reflection as a direct biochemical assay technique," Sens. Actuators B **81**, 316–328 (2002).
6. J. J. Wang, L. Chen, S. Kwan, F. Liu, and X. Deng, "Resonant grating filters as refractive index sensors for chemical and biological detections," J. Vac. Sci. Technol. B **23**, 3006–3010 (2005).
7. K. J. Lee, D. Wawro, P. S. Priambodo, and R. Magnusson, "Agarose-gel-based guided-mode resonance humidity sensor," IEEE Sens. J. **7**, 409–414 (2007).
8. R. Magnusson, D. Wawro, S. Zimmerman, Y. Ding, M. Shokooh-Saremi, K. J. Lee, D. Ussery, S. Kim, and S. H. Song, "Leaky-mode resonance photonics: technology for biosensors, optical components, MEMS, and plasmonics," Proc. SPIE **7604**, 76040M (2010).
9. K. J. Lee, J. Jin, B.-S. Bae, and R. Magnusson, "Optical filters fabricated in hybrimer media with soft lithography," Opt. Lett. **34**, 2510–2512 (2009).
10. J. Viheriala, T. Niemi, J. Laukkanen, M. Karjalainen, and M. Pessa, "Large-area nanoperforated SiN membranes for optical and mechanical filtering," Microelectron. Eng. **87**, 1620–1622 (2010).
11. S. Wei and F. Li, "Measurement of photoresist grating profiles based on multiwavelength scatterometry and artificial neural network," Appl. Opt. **47**, 2524–2532 (2008).
12. International Technology Roadmap for Semiconductors, http://www.itrs.net/Links/2009ITRS/Home2009.htm (2009).
13. T. Schuster, S. Rafler, V. F. Paz, K. Frenner, and W. Osten, "Fieldstitching with Kirchhoff-boundaries as a model-based description for line edge roughness (LER) in scatterometry," Microelectron. Eng. **86**, 1029–1032 (2009).
14. B. C. Bergner, T. A. Germer, and T. J. Suleski, "Effective medium approximations for modeling optical reflectance from gratings with rough edges," J. Opt. Soc. Am. A **27**, 1083–1090 (2010).
15. A. Talneau, F. Lemarchand, A.-L. Fehrembach, and A. Sentenac, "Impact of electron-beam lithography irregularities across millimeter-scale resonant grating filter performances," Appl. Opt. **49**, 658–662 (2010).
16. M. K. Poutous, Z. Roth, K. Buhl, A. Pung, R. C. Rumpf, and E. G. Johnson, "Correlation of fabrication tolerances with the performance of guided-mode-resonance micro-optical components," Proc. SPIE **7205**, 72050Y (2009).
17. T. Prasad, V. L. Colvin, and D. M. Mittleman, "Effect of structural disorder on guided resonances in photonic crystal slabs studied with terahertz time-domain spectroscopy," Opt. Express **15**, 16954–16965 (2007).
18. L. Li, "New formulation of the Fourier modal method for crossed surface-relief gratings," J. Opt. Soc. Am. A **14**, 2758–2767 (1997).
19. M. G. Moharam, D. A. Pommet, E. B. Grann, and T. K. Gaylord, "Stable implementation of the rigorous coupled-wave analysis for surface-relief gratings—enhanced transmittance matrix approach," J. Opt. Soc. Am. A **12**, 1077–1086 (1995).
20. M. G. Moharam, E. B. Grann, D. A. Pommet, and T. K. Gaylord, "Formulation for stable and efficient implementation of the rigorous coupled-wave analysis of binary gratings," J. Opt. Soc. Am. A **12**, 1068–1076 (1995).
21. K. J. Lee, R. LaComb, B. Britton, M. Shokooh-Saremi, H. Silva, E. Donkor, Y. Ding, and R. Magnusson, "Silicon-layer guided-mode resonance polarizer with 40 nm bandwidth," IEEE Photon. Technol. Lett. **20**, 1857–1859 (2008).
22. D. H. Shin, S. Tibuleac, T. A. Maldonado, and R. Magnusson, "Thin-film optical filters with diffractive elements and waveguides," Opt. Eng. **37**, 2634–2646 (1998).
23. V. Constantoudis, G. P. Patsis, L. H. A. Leunissen, and E. Gogolides, "Towards a complete description of line width roughness: a comparison of different methods for vertical and spatial LER and LWR analysis and CD variation," Proc. SPIE **5375**, 967–977 (2004).
24. D. Marcuse, "Theory of dielectric optical waveguides," in *Quantum Electronics—Principles and Applications* (Academic, 1991).
25. T. A. Germer, "Effect of line and trench profile variation on specular and diffuse reflectance from a periodic structure," J. Opt. Soc. Am. A **24**, 696–701 (2007).
26. E. Gogolides, V. Constantoudis, G. P. Patsis, and A. Tserepi, "A review of line edge roughness and surface nanotexture resulting from patterning processes," Microelectron. Eng. **83**, 1067–1072 (2006).
27. I. Abdulhalim, "Simplified optical scatterometry for periodic nanoarrays in the near-quasi-static limit," Appl. Opt. **46**, 2219–2228 (2007).